Polarized excitons and optical activity in single-wall carbon nanotubes

Yao-Wen Chang* and Bih-Yaw Jin†

Department of Chemistry and Center for Emerging Material and Advanced Devices and Center for Quantum Science and Engineering, National Taiwan University, Taipei 10617, Taiwan

(Received 8 August 2017; revised manuscript received 12 April 2018; published 9 May 2018)

The polarized excitons and optical activity of single-wall carbon nanotubes (SWNTs) are studied theoretically by π-electron Hamiltonian and helical-rotational symmetry. By taking advantage of the symmetrization, the single-particle energy and properties of a SWNT are characterized with the corresponding helical band structure. The dipole-moment matrix elements, magnetic-moment matrix elements, and the selection rules can also be derived. Based on different selection rules, the optical transitions can be assigned as the parallel-polarized, left-handed circularly-polarized, and right-handed circularly-polarized transitions, where the combination of the last two gives the cross-polarized transition. The absorption and circular dichroism (CD) spectra are simulated by exciton calculation. The calculated results are well comparable with the reported measurements. Built on the foundation, magnetic-field effects on the polarized excitons and optical activity of SWNTs are studied. Dark-bright exciton splitting and interband Faraday effect in the CD spectrum of SWNTs under an axial magnetic field are predicted. The Faraday rotation dispersion can be analyzed according to the selection rules of circular polarizations and the helical band structure.

DOI: 10.1103/PhysRevB.97.205413

I. INTRODUCTION

Single-wall carbon nanotubes (SWNTs) are quasi-one-dimensional nanomaterials that are known for their unique physical properties [1–5]. Particularly, a semiconducting SWNT shows excitonic effect in the absorption and emission spectra, where the resonance frequency and intensity depend upon the corresponding geometry and physical environment [6–17]. The unique properties make semiconducting SWNTs promising materials for designing future nanoscale photodetectors and photoemitters.

The chiral index (n,m) characterizes the geometry and symmetry of a SWNT. A carbon nanotube is classified as zigzag if its chiral index is $(n,0)$, armchair if its index is (n,n), and chiral otherwise. A material is called chiral if the material has an enantiomer, which is the mirror image of the material that is not superposable on its mirror image. Chiral materials, including chiral SWNTs, are optically active. It means that the absorption intensities of left-handed circularly polarized light and right-handed circularly polarized light through the material are different, and circular dichroism (CD) is a spectroscopy to measure the difference [18–21]. Today, thanks to the progress of experimental technologies, high-purity single-chirality enantiomers of SWNTs have been separated and chiral-specified CD spectra have been measured [22–27]. It is now possible to use the CD spectra to benchmark the theoretical studies. Challenging issues of optical activity in SWNTs can be asked and answered.

An important issue of optical activity in SWNTs is to identify different contributions of polarized excitons to the CD spectrum. It is known that the optical transitions of SWNTs are known to be highly anisotropic [15,28,29]. The electromagnetic-field interaction that polarized parallelly and perpendicularly to the nanotube axis give distinct spectra. From the point of view of band-to-band transition under zone-folding approximation or effective-mass approximation, the vertical transition between the Nth valence band beneath and the Nth conduction band above the Fermi energy can be assigned as the parallel-polarized transition, while the vertical transitions between the Nth valence band and the $(N \pm 1)$th conduction bands can be assigned as the cross-polarized (also known as perpendicular-polarized) transitions [15,28,29]. For semiconducting SWNTs, the lowest resonant energy of cross-polarized transition (E_{12}) is slightly higher than the middle of the first (E_{11}) and second (E_{22}) lowest resonant energies of parallel-polarized transitions [28–30]. Theoretical studies have predicted that the cross-polarized transition is sensitive to electron-electron interaction, electron-hole asymmetry, and environmental interaction in SWNTs [31–33], thus becoming a useful tool to analyze the electronic structures and excitonic effects of SWNTs [34,35]. For CD spectrum, the resonant energies of polarized excitons can still be interpreted by the band-to-band polarized transitions [27], but the signs and intensities in CD spectrum are less explicit to understand and study. An alternative point of view might be wanted.

Another issue of optical activity in SWNTs is the magnetic-field effects. Particularly, by applying a uniform magnetic field parallel to the axial direction of an SWNT, the electronic states change with varying magnetic flux due to Aharonov-Bohm effect [36–40]. Although the band structure of a small-radius SWNT can have a measurable change only by imposing extremely high magnetic field, the Aharonov-Bohm effect can be observed in optical spectra as the emerging dark-exciton resonance transitions with an experimentally accessible

*yaowen920@gmail.com
†byjin@ntu.edu.tw

magnetic field due to the inversion symmetry breaking. While the emerging dark exciton has been studied extensively in theoretical simulation [38–40] and experimental measurement [41–45] of absorption spectrum and photoluminescence, the Aharonov-Bohm effect is also expected to be observed in CD spectrum. Therefore, a new question can be asked: What is the optical activity of dark-exciton states in SWNTs. An answer to the question may help us to advance the knowledge of the Aharonov-Bohm effect in SWNTs.

Except the emerging dark exciton, Faraday rotation in SWNTs has also been predicted to be observed under an axial magnetic field in CD spectrum of cross-polarized exciton [46–49] due to an interband Faraday effect [50–52]. In such cases, the difference in right-handed and left-handed circularly-polarized transitions can be attributed to the magnetic-field-induced band structure distortion and handedness-selected transitions, instead of the intrinsic chirality of the SWNT. Therefore, the Faraday rotation dispersion can provide extra information on the relationship between the optical activity and the electronic structure. The handedness of cross-polarized excitons can also be identified.

Some theoretical studies on optical activity and CD spectrum of SWNTs have been published [53–56]. However, the excitonic effect on the CD spectrum has only been discussed limitedly, and to describe the CD spectra of SWNTs accurately is still difficult. In most theoretical studies, the band structures and exciton spectra of chiral SWNTs are calculated under translational symmetry with zone-folding approximation or effective-mass approximation. Despite that the exciton binding energy and the parallel-polarized transitions can be simulated well [13,15], these methods ignore the intrinsic helical symmetry (also known as screw symmetry) of chiral SWNTs, thus either oversimplifying the geometrical information to study chirality-sensitive properties or complicating the mathematics for simulating CD spectrum. In fact, if the helical symmetry is used to analyze the geometry of a chiral SWNT, we can find that a chiral SWNT can be seen as several interconnected helical polyacetylenes. Helical polymers are one of the most extensively studied optically-active materials since DNA and polypeptide are sorted into this category [57], and most theoretical studies take helical symmetry as a start to study the optical spectra [58–62]. Therefore, it is reasonable to assume that SWNTs can also be studied and analyzed with the same methodology and interpretation. In some reports, the helical symmetry has been applied to the study of band structures [11,63–66] and optical spectra of SWNTs [11]. However, the applications to cross-polarized transition and CD spectrum have not been discussed. Without using helical symmetry, the unit cell of a chiral SWNT normally contains too many atoms to make the calculation of the exciton spectra efficiently and accurately. It is a gap we intend to fill.

A helical symmetry can be realized as a finite distance of translation accompanying with a finite angle of rotation. The structure of a helical polymer which fulfills helical symmetry can be described by the coordinate

$$\mathbf{R}(r) = \rho_0 \cos(r\phi_{\mathrm{H}})\mathbf{e}_1 + \rho_0 \sin(r\phi_{\mathrm{H}})\mathbf{e}_2 + r z_{\mathrm{H}}\mathbf{e}_3, \quad (1)$$

where $\mathbf{e}_1$, $\mathbf{e}_2$, $\mathbf{e}_3$ are the basis vectors of Cartesian coordinate, ρ_0 is the radius of the helix, ϕ_{H} and z_{H} are the helical angle and the displacement, which are the rotational part and translational part of a helical transformation, and r is a parameter indicating the position in the spiral. For a function of the position vector $f(\mathbf{R})$, by the Born-von-Karman boundary condition $\mathbf{R}(r+N) = \mathbf{R}(r)$, the Fourier transform is given by

$$\tilde{f}_\kappa = \frac{1}{\sqrt{N}} \sum_{r=0}^{N-1} f(\mathbf{R}(r)) \exp(-\mathrm{i}\kappa r), \quad (2)$$

where $\kappa = 2\pi K/N$ (with $K = 0, 1, \cdots, N-1$) is called helical momentum. Similar to the quasimomentum in solid-state physics, helical momentum can be applied to the interpretation of band structures and optical transitions of helical polymers. By the Fourier transform, the selection rule of parallel-polarized transition can be found as

$$\Delta\kappa = 0, \quad (3)$$

and the selection rule of cross-polarized transition can be found as

$$\Delta\kappa = \pm\phi_{\mathrm{H}}. \quad (4)$$

The first selection rule is known as the vertical transition in energy band theory, which is well studied in the extended system. The second selection rule, however, is less recognized in the theoretical studies of the optical spectra of SWNTs, since the rule is absent in conventional translational-symmetry paradigm. In fact, the selection rule was proposed as early as 1953 by Higgs [58], right after the helical structure of polypeptide was found [57]. The selection rule has been rediscovered and applied to the simulation of the CD spectra of helical polymers [59–62]. The selection rule is not only conveniently providing a useful method to calculate the cross-polarized transition in exciton spectra, but also showing an intriguing structure-property relationship of helical structure. With the background, the helical symmetry and the selection rules might be worth a review as a renewed concept in the research of SWNTs.

In the present study, the polarized excitons in absorption and CD spectra of chiral SWNTs are simulated and studied by using helical-rotational symmetry on the band structure calculation under Hartree-Fock approximation and the exciton calculation under singly-excited configuration interaction approximation. We use the Pariser-Parr-Pople (PPP) Hamiltonian [32,67–69], which is a pure π-electron model with both short-range and long-range Coulomb interaction, to simulate the electronic structures. At least 3600 two-atomic unit cells are used to construct the helical band structures and the exciton wave functions. Each helical band structure is characterized by a helical momentum (κ) and a circumferential angular momentum (λ). According to the selection rules derived, the optical transitions can be assigned as the parallel-polarized transition ($\Delta\kappa = 0$, $\Delta\lambda = 0$), left-handed circularly-polarized transition ($\Delta\kappa = \phi_{\mathrm{H}}$, $\Delta\lambda = 1$), and right-handed circularly-polarized transition ($\Delta\kappa = -\phi_{\mathrm{H}}$, $\Delta\lambda = -1$). The combination of the two handed circularly-polarized transitions gives the cross-polarized transition. By this scheme, the interplay of polarized excitons, optical activity, and magnetic-field effects in SWNTs is studied and discussed.

The paper is organized as follows. In Sec. II A, the Hamiltonian is written in second quantized form, and the way to include the static magnetic field interaction is introduced.

Then the light-matter interaction of the model and the formula to calculate the absorption and CD spectra are introduced in Sec. II B. In Sec. II C, we give the method to generate the coordinate of each lattice point in a SWNT by using helical-rotational construction. By using the coordinate, in Sec. II D, the helical band structure of a SWNT with an axially uniform magnetic field is solved analytically. In Sec. II E, the dipole-moment and magnetic-moment matrix elements of both the parallel-polarized and cross-polarized transitions are derived. The selection rules are shown. In Sec. II F, the formulations of Hartree-Fock equation and singly-excited configuration interaction are given. In Sec. III, the calculated results are presented. In Secs. III A and III B, the simulated absorption and CD spectra are compared with the experimental measurements. The Aharonov-Bohm effect of dark exciton is discussed in Sec. III C, and the Faraday effect on the cross-polarized transition is discussed in Sec. III D. Finally, in Sec. IV, the present paper is concluded.

II. THEORY

A. Hamiltonian

The tight-binding Hamiltonian for π-electron systems with orthogonal bases is also known as Hückel Hamiltonian and is very useful in the study of the physical properties of conjugated systems [69]. With the lattice basis, the Hamiltonian in the presence of an external magnetic field can be written as

$$\hat{\mathcal{H}}_{\rm TB} = \sum_{\mathbf{R}_1\mu,\mathbf{R}_2\nu} \hat{T}_{\mathbf{R}_1\mu,\mathbf{R}_2\nu}, \tag{5}$$

$$\hat{T}_{\mathbf{R}_1\mu,\mathbf{R}_2\nu} = \mathrm{e}^{\mathrm{i}e\int_{\mathbf{R}_{2\nu}}^{\mathbf{R}_{1\mu}} \mathrm{d}\mathbf{r}\cdot\boldsymbol{\mathcal{A}}(\mathbf{r})} \sum_{\alpha} h_{\mathbf{R}_1\mu,\mathbf{R}_2\nu} \hat{a}^{\dagger}_{\mathbf{R}_1\mu\alpha} \hat{a}_{\mathbf{R}_2\nu\alpha}, \tag{6}$$

where $\hat{a}^{\dagger}_{\mathbf{R}_1\mu\alpha}/\hat{a}_{\mathbf{R}_1\mu\alpha}$ is the Fermi creation/annihilation operator of an electron at site μ of unit cell at position $\mathbf{R}_1$ with spin index $\alpha = \{\uparrow,\downarrow\}$, $\mathbf{R}_{1\mu} = \mathbf{R}_1 + \mathbf{d}_\mu$ is the position vector, with $\mathbf{R}$ the position vector of the unit cell and $\mathbf{d}_\mu$ the basis vector inside the unit cell, $\boldsymbol{\mathcal{A}}(\mathbf{r})$ is the vector potential, e is the charge, and the hopping term

$$h_{\mathbf{R}_1\mu,\mathbf{R}_2\nu} = \begin{cases} -t, & \mathbf{R}_{1\mu},\mathbf{R}_{2\nu} \text{ nearest neighbor} \\ -t', & \mathbf{R}_{1\mu},\mathbf{R}_{2\nu} \text{ next nearest neighbor} \\ 0, & \text{otherwise} \end{cases}$$

with t and t' the nearest-neighbor and next-nearest-neighbor hopping coupling. The exponential part is called the Peierls phase factor [70]. The Fermi operators fulfill the anticommutation relation $\{\hat{a}_{\mathbf{R}_1\mu\alpha},\hat{a}^{\dagger}_{\mathbf{R}_2\nu\beta}\} = \delta_{\mathbf{R}_1\mathbf{R}_2}\delta_{\mu\nu}\delta_{\alpha\beta}$, which implies the orthogonality of the basis. If the π-electron system interacts with a uniform magnetic field, by using symmetric Coulomb gauge, the vector potential is given by

$$\boldsymbol{\mathcal{A}}(\mathbf{r}) = -\tfrac{1}{2}(\mathbf{r}-\mathbf{R}_0)\times\boldsymbol{\mathcal{B}}, \tag{7}$$

with $\boldsymbol{\mathcal{B}}$ and $\mathbf{R}_0$ being the uniform magnetic field and the gauge origin, respectively. Set $\mathbf{R}_0 = 0$, the phase factor can be rewritten as

$$\mathrm{i}e\int_{\mathbf{R}_{2\nu}}^{\mathbf{R}_{1\mu}} \mathrm{d}\mathbf{r}\cdot\boldsymbol{\mathcal{A}}(\mathbf{r}) = -\frac{\mathrm{i}e}{2}(\mathbf{R}_{1\mu}\times\mathbf{R}_{2\nu})\cdot\boldsymbol{\mathcal{B}}. \tag{8}$$

The PPP Hamiltonian adds the Coulomb interaction to the tight-binding Hamiltonian $\hat{\mathcal{H}}_{\rm PPP} = \hat{\mathcal{H}}_{\rm TB} + \hat{\mathcal{V}}_{\rm C}$, where the Coulomb interaction is given by [32,69]

$$\hat{\mathcal{V}}_{\rm C} = U\sum_{\mathbf{R},\mu}\left(\hat{n}_{\mathbf{R}\mu\uparrow}-\frac{1}{2}\right)\left(\hat{n}_{\mathbf{R}\mu\downarrow}-\frac{1}{2}\right) + \frac{1}{2}\sum_{\mathbf{R}_{1\mu}\neq\mathbf{R}_{2\nu}} \frac{e^2\hat{Q}_{\mathbf{R}_1\mu}\hat{Q}_{\mathbf{R}_2\nu}}{\epsilon_{\rm r}\sqrt{(e^2/U)^2+|\mathbf{R}_{1\mu}-\mathbf{R}_{2\nu}|^2}}, \tag{9}$$

where $\hat{n}_{\mathbf{R}\mu\alpha} = \hat{a}^{\dagger}_{\mathbf{R}\mu\alpha}\hat{a}_{\mathbf{R}\mu\alpha}$ is the site electron density, and $\hat{Q}_{\mathbf{R}\mu} = \sum_\alpha \hat{n}_{\mathbf{R}\mu\alpha} - 1$ is the site charge density. The parameter U is on-site Coulomb coupling, $\epsilon_{\rm r}$ is a dielectric constant which parametrizes environmental interaction and σ-electron polarization, and $e^2 = 14.397$ eV Å is the coupling strength.

B. Optical absorption and circular dichroism

To calculate the optical absorption and CD of SWNTs, we use standard multipole-moment expansion of light-matter interaction to derive the (electric) dipole-moment and magnetic-moment operators under tight-binding approximation and then use the operators and sum-over-state formula to find the transition intensities. The light-matter interaction adding to the electronic Hamiltonian under tight-binding basis ($\hat{\mathcal{H}}' = \hat{\mathcal{H}}_{\rm PPP} + \hat{\mathcal{V}}_{\rm LM}$) can also be written as the Peierls phase factor of the hopping interaction [71]. The light-matter interaction is written

$$\hat{\mathcal{V}}_{\rm LM} = \sum_{\mathbf{R}_1\mu,\mathbf{R}_2\nu} [\mathrm{e}^{\mathrm{i}e\int_{\mathbf{R}_{2\nu}}^{\mathbf{R}_{1\mu}}\mathrm{d}\mathbf{r}\cdot\boldsymbol{\mathcal{A}}_{\rm L}(\mathbf{r})} - 1]\hat{T}_{\mathbf{R}_1\mu,\mathbf{R}_2\nu}, \tag{10}$$

where $\boldsymbol{\mathcal{A}}_{\rm L}(\mathbf{r})$ is the vector potential of light, given that the Coulomb gauge is chosen. The vector potential can be written as the plane-wave expansion

$$\boldsymbol{\mathcal{A}}_{\rm L}(\mathbf{r}) = \sum_I \int \frac{\mathrm{d}^3k}{(2\pi)^3}\mathbf{e}_I\tilde{\mathcal{A}}^I_{\rm L}(\mathbf{k})\mathrm{e}^{-\mathrm{i}\mathbf{k}\cdot(\mathbf{r}-\mathbf{R}_0)}, \tag{11}$$

where $\mathbf{e}_I$ is polarization vector, and $\mathbf{R}_0$ is the gauge origin. Although SWNTs are thought to be one-dimensional solids and the electromagnetic field interaction should be nonlocal, the wavelength of the characteristic electronic absorption is on the scale of a few hundred nanometers and is long enough that SWNTs shorter than the length can still be treated as solids. Therefore, the long-wavelength approximation can still be applied and the nonlocal effect can be ignored. By the expansion of the exponential factor in Eq. (11),

$$\mathrm{e}^{-\mathrm{i}\mathbf{k}\cdot(\mathbf{r}-\mathbf{R}_0)} = 1 - \mathrm{i}\mathbf{k}\cdot(\mathbf{r}-\mathbf{R}_0) + \cdots, \tag{12}$$

and set $\mathbf{R}_0 = 0$, the light-matter interaction can be given by the dipole-moment approximation,

$$\hat{\mathcal{V}}_{\rm LM} \simeq -\hat{\boldsymbol{\mu}}\cdot\boldsymbol{\mathcal{E}}_{\rm L} - \hat{\mathbf{m}}\cdot\boldsymbol{\mathcal{B}}_{\rm L} + \cdots, \tag{13}$$

where $\boldsymbol{\mathcal{E}}_{\rm L} = -\mathrm{d}\boldsymbol{\mathcal{A}}_{\rm L}/\mathrm{d}t$ is the transverse electric field and $\boldsymbol{\mathcal{B}}_{\rm L} = \nabla\times\boldsymbol{\mathcal{A}}_{\rm L}$ is the magnetic field. The dipole-moment operator is [72,73] (also see the Supplemental Material [74])

$$\hat{\boldsymbol{\mu}} = e\sum_{\mathbf{R}\mu}\sum_{\alpha}\mathbf{R}_\mu\hat{a}^{\dagger}_{\mathbf{R}\mu\alpha}\hat{a}_{\mathbf{R}\mu\alpha}, \tag{14}$$

and the magnetic-moment operator is

$$\hat{\mathbf{m}} = \frac{\mathrm{i}e}{2} \sum_{\mathbf{R}_{1\mu},\mathbf{R}_{2\nu}} (\mathbf{R}_{1\mu} \times \mathbf{R}_{2\nu}) \hat{T}_{\mathbf{R}_{1\mu},\mathbf{R}_{2\nu}}. \tag{15}$$

The magnetic-moment operator can also be found by $\hat{m}_i = -\partial \hat{\mathcal{H}}_{\mathrm{TB}}/\partial \mathcal{B}_i$, except that the magnetic-moment operator is induced by static field instead of light. The magnetic-moment operator derived from static-field interaction and light-matter interaction share the same formula, but the difference should be noticed. It is also needed to note that the magnetic-moment approximation is no longer gauge invariant. With different gauge origin $\mathbf{R}_0$, the calculated spectra would be different. However, it is a reasonable approximation to define $\mathbf{R}_0$ at a point on the axis of an SWNT, since the magnetic moment can be seen as the inductive magnetic field generated by the electric current flowing spirally as an electric coil along the SWNT. The effect of gauge dependence is weak and can be ignored in this paper.

Under the light-matter interaction, the first-order variations of the polarization ($\tilde{\boldsymbol{\mu}} \equiv \langle \hat{\boldsymbol{\mu}} \rangle$) with respect to the electromagnetic field is [18–21]

$$\tilde{\mu}^I(\omega) = \sum_J \alpha^{IJ}(-\omega;\omega)\mathcal{E}^J_{\mathrm{L}}(\omega) + \mathrm{i}\omega \sum_J G^{IJ}(-\omega;\omega)\mathcal{B}^J_{\mathrm{L}}(\omega) + \cdots, \tag{16}$$

where $\alpha^{IJ}(-\omega;\omega)$ is the electric polarizability, $G^{IJ}(-\omega;\omega)$ is the electric-magnetic polarizability, and $I,J = \{1,2,3\}$ indicates the basis of the Cartesian coordinate. By time-dependent perturbation theory, the linear polarizability is given by the sum-over-state expression [71]

$$\alpha^{IJ}(-\omega;\omega) = \sum_M \left(\frac{\mu^I_{0M}\mu^J_{M0}}{\omega_{M0} - \omega} + \frac{\mu^J_{0M}\mu^I_{M0}}{\omega^*_{M0} + \omega} \right), \tag{17}$$

where $\mu^I_{0M} = \langle \Phi_0 | \hat{\mu}^I | \Phi_M \rangle$, $\omega_{M0} = E_M - E_0 - \mathrm{i}\eta$, with E_M the eigenenergy of the Mth excited state, E_0 the ground state energy, and η the line-broadening factor. The electric-magnetic polarizability can also be given by the sum-over-state expression [18,21]

$$G^{IJ}(-\omega;\omega) = \sum_M \frac{1}{\omega_{M0}} \left[\frac{\mathrm{Im}(\mu^I_{0M} m^J_{M0})}{\omega_{M0} - \omega} - \frac{\mathrm{Im}(m^J_{0M}\mu^I_{M0})}{\omega^*_{M0} + \omega} \right], \tag{18}$$

where $m^I_{0M} = \langle \Phi_0 | \hat{m}^I | \Phi_M \rangle = -m^I_{M0}$. By using Eq. (16) and Maxwell's equation, the dependence of reflection index with the two polarizabilities can be found, and then the absorption intensity and the rotatory power can be related to them.

Suppose that a SWNT is aligned vertically alone with the $\mathbf{e}_3$ direction. The parallel-polarized transition in the absorption spectrum is given by

$$\epsilon_{\mathrm{PP}}(\omega) = \nu_0 \omega \ \mathrm{Im}\, \alpha^{33}(-\omega;\omega), \tag{19}$$

with $\omega \geqslant 0$, where $\nu_0 = 1.085 \times 10^{11} \times 8065.544 \times 10^{-16}$ is a factor to scale the absorption intensity by the unit of oscillator strength density, within the formula the unit of energy being eV, the unit of length being Å, and the charge $|e| = 1$ being presumed [69]. The cross-polarized transition in the absorption spectrum is given by

$$\epsilon_{\mathrm{CP}}(\omega) = \nu_0 \omega \ \mathrm{Im}[\alpha^{11}(-\omega;\omega) + \alpha^{22}(-\omega;\omega)]. \tag{20}$$

The parallel-polarized transition in CD spectrum is given by [18,19,21]

$$\Delta\epsilon_{\mathrm{PP}}(\omega) = \frac{\nu_0 \omega^2}{\mathrm{c}_0} \mathrm{Im}\ G^{33}(-\omega;\omega), \tag{21}$$

where c_0 is the velocity of light and is approximated by $\mathrm{c}_0 \simeq 137$. With the formula, the CD spectrum is measured by rotational strength density. On the other hand, the cross-polarized transition in CD spectrum can be separated into two major contributions $\Delta\epsilon_{\mathrm{CP}}(\omega) = \Delta\epsilon_{\mathrm{CP},1}(\omega) + \Delta\epsilon_{\mathrm{CP},2}(\omega)$, where (see the Supplemental Material [74])

$$\Delta\epsilon_{\mathrm{CP},1}(\omega) = \frac{\nu_0 \omega^2}{\mathrm{c}_0} \mathrm{Im}[G^{11}(-\omega;\omega) + G^{22}(-\omega;\omega)], \tag{22}$$

$$\Delta\epsilon_{\mathrm{CP},2}(\omega) = \nu_0 \omega \mathrm{Re}[\alpha^{12}(-\omega;\omega) - \alpha^{21}(-\omega;\omega)]. \tag{23}$$

The second contribution is normally known as the Faraday effect. In the contribution, $\Delta\epsilon_{\mathrm{CP},2}(\omega)$ can be measured only if both the polarization vectors have components on the surface spanned by $\mathbf{e}_1$ and $\mathbf{e}_2$, and there exist magnetic fields or other time-reversal-symmetry-breaking interactions [48,50–52]. While the rotational strength of CD spectrum is only contributed from Eq. (22) in zero magnetic field, the contribution from Eq. (23) usually becomes dominant for most materials with increasing finite magnetic field due to the factor of c_0 difference between the two formulas.

C. Symmetry and geometry of SWNTs

The chiral vector of an SWNT with chiral number (n,m) is defined as $\mathbf{C}_h = n\mathbf{a}_1 + m\mathbf{a}_2$, where $\mathbf{a}_1$ and $\mathbf{a}_2$ are the lattice vectors. The length of the chiral vector $|\mathbf{C}_h| = a_0\sqrt{n^2 + m^2 + nm}$ is also the circumference of the SWNT. The translational vector is given by $\mathbf{T} = t_1\mathbf{a}_1 + t_2\mathbf{a}_2$, with $t_1 = (2m + n)/d_R$ and $t_2 = -(2n + m)/d_R$, where d_R is the greatest common divisor (GCD) of $(2n + m, 2m + n)$ [1]. Although the translational vector and the chiral vector can be used to generate the coordinates of all lattice points and to construct the band structures, it is much simpler and computationally less costly to work within the helical-rotational construction [63–65]. The basis of the helical-rotational construction consists of the helical vector $\mathbf{H}$ and the rotational vector given by $\mathbf{C}$ [63]

$$\boldsymbol{\tau}_1 = \mathbf{H} = h_1\mathbf{a}_1 + h_2\mathbf{a}_2, \tag{24}$$

$$\boldsymbol{\tau}_2 = \mathbf{C} = \frac{n}{d}\mathbf{a}_1 + \frac{m}{d}\mathbf{a}_2, \tag{25}$$

where d is the GCD of the chiral number (n,m). The helical index (h_1,h_2) is chosen to be the minimum integer numbers to fulfill $|h_1 m - h_2 n| = d$ with $h_1,h_2 \geqslant 0$. In the following paragraphs of this section, we will give details of how to generate the lattice points by using the helical-rotational construction, and in Sec. II D we will use these symmetry operations to construct the band structure. In Fig. 1, the vectors of a (6,4)-SWMT are shown. The dash-line indicates the route that a lattice point will pass in the direction along the helical

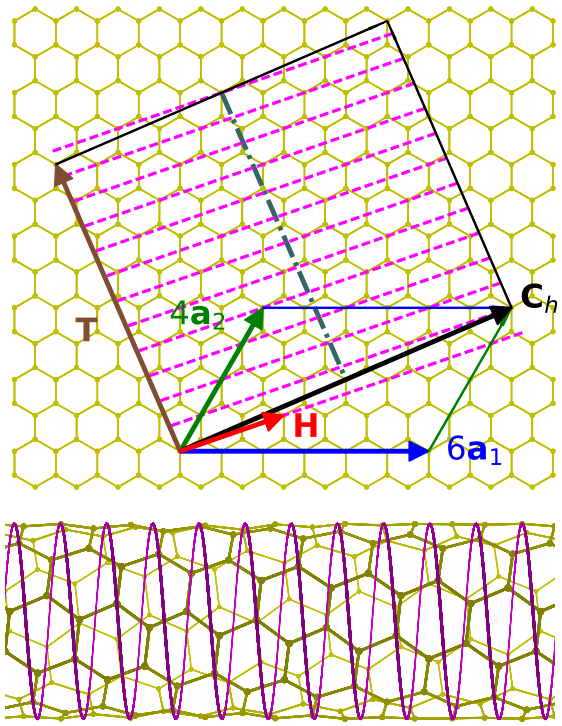

FIG. 1. Symmetry and geometry of unrolled (up) and rolled-up (down) (6,4)−SWNT.

vector. The dash-dot line partitions the unrolled SWNT into two equivalent cells which can be transformed to each other by the twofold rotational symmetry operation.

In order to describe the geometry and derive the dipole-moment/magnetic-moment matrix elements of SWNTs, we need to know the position vector $\mathbf{R}_\mu$ of each lattice point. To do so, we first turn to find the position vector $\boldsymbol{\mathcal{R}}_\mu$ of each lattice point in an unrolled SWNT, which is actually a plane graphene sheet as shown in Fig. 1. After finding each $\boldsymbol{\mathcal{R}}_\mu$, we can use the coordinate chart of cylindrical surface to find the one-to-one map of the lattice points on the unrolled SWNT to the lattice points on the rolled-up SWNT, and then we can generate the position vector $\mathbf{R}_\mu$.

The position vectors of lattice points in an unrolled SWNT $\boldsymbol{\mathcal{R}}_\mu$, with $\mu = \{A,B\}$ indicating the two atoms in a unit cell, are given by $\boldsymbol{\mathcal{R}}_A = \boldsymbol{\mathcal{R}} + \mathbf{b}_0$ and $\boldsymbol{\mathcal{R}}_B = \boldsymbol{\mathcal{R}}$, where $\boldsymbol{\mathcal{R}}$ is the position vector of a unit cell and $\mathbf{b}_0$ is the basis vector linking the two carbon atoms in the unit cell. The position vector can be defined by using lattice-vector construction $\boldsymbol{\mathcal{R}}(p,q) = p\mathbf{a}_1 + q\mathbf{a}_2$ or using helical-rotational construction $\boldsymbol{\mathcal{R}}(r,s) = r\boldsymbol{\tau}_1 + s\boldsymbol{\tau}_2$. By a direct substitution, the position vector in lattice-vector construction can be transformed to the one in helical-rotational construction by

$$\begin{aligned}\boldsymbol{\mathcal{R}}(r,s) &= p(r,s)\mathbf{a}_1 + q(r,s)\mathbf{a}_2 \\ &= \left(rh_1 + \frac{sn}{d}\right)\mathbf{a}_1 + \left(rh_2 + \frac{sm}{d}\right)\mathbf{a}_2. \end{aligned} \tag{26}$$

The reversed transformation is

$$\begin{aligned}\boldsymbol{\mathcal{R}}(p,q) &= r(p,q)\boldsymbol{\tau}_1 + s(p,q)\boldsymbol{\tau}_2 \\ &= \frac{pm - qn}{D}\boldsymbol{\tau}_1 + \frac{d(h_1 q - h_2 p)}{D}\boldsymbol{\tau}_2, \end{aligned} \tag{27}$$

where $D = h_1 m - h_2 n$. We can find $D = \pm d$ for different SWNTs and chosen helical indices.

By using the coordinate chart of the cylindrical surface, the position vectors of the lattice points in a rolled-up SWNT can be parametrized by the lattice-vector construction as

$$\begin{aligned}\mathbf{R}(p,q) &= \rho_0 \cos(p\phi_1 + q\phi_2)\mathbf{e}_1 + \rho_0 \sin(p\phi_1 + q\phi_2)\mathbf{e}_2 \\ &\quad + (pz_1 + qz_2)\mathbf{e}_3, \end{aligned} \tag{28}$$

where $\rho_0 = |\mathbf{C}_h|/2\pi$ is the radius of the tube, $\phi_\sigma = 2\pi a_0 \cos\Phi_\sigma/|\mathbf{C}_h|$ and $z_\sigma = a_0 \sin\Phi_\sigma$, with Φ_1 and Φ_2 being chiral angles and given by $\cos\Phi_\sigma = \mathbf{C}_h \cdot \mathbf{a}_\sigma/(|\mathbf{C}_h||\mathbf{a}_\sigma|)$. By using the transformation in Eq. (26), the position vector of the lattice point parametrized by the helical-rotational construction can be found as

$$\mathbf{R}(r,s) = \rho_0 \cos(\boldsymbol{\mathcal{R}} \cdot \boldsymbol{\phi})\mathbf{e}_1 + \rho_0 \sin(\boldsymbol{\mathcal{R}} \cdot \boldsymbol{\phi})\mathbf{e}_2 + r z_{\mathrm{H}} \mathbf{e}_3, \tag{29}$$

where

$$\boldsymbol{\phi} = \frac{\phi_{\mathrm{H}}}{2\pi}\mathbf{g}_1 + \frac{\phi_{\mathrm{R}}}{2\pi}\mathbf{g}_2, \tag{30}$$

and

$$\phi_{\mathrm{H}} = \pi \frac{h_1(2n+m) + h_2(2m+n)}{n^2 + m^2 + nm}, \tag{31}$$

$$z_{\mathrm{H}} = \frac{\sqrt{3}a_0 D}{2\sqrt{n^2 + m^2 + nm}}, \tag{32}$$

$$\phi_{\mathrm{R}} = \frac{2\pi}{d} \tag{33}$$

are helical angle, displacement, and rotational angle, respectively. The reciprocal-lattice vectors $\mathbf{g}_j$ are defined by [65]

$$\boldsymbol{\tau}_i \cdot \mathbf{g}_j = 2\pi\delta_{ij}, \tag{34}$$

such that $\boldsymbol{\mathcal{R}} \cdot \boldsymbol{\phi} = r\phi_{\mathrm{H}} + s\phi_{\mathrm{R}}$. The formula of position vector in Eq. (29) is a very simple method to generate the coordinates of all the lattice points of $\mathbf{R}_B(r,s)$ with $r = 0,1,\ldots,N-1$ and $s = 0,1,\ldots,d-1$. To generate the coordinate of each $\mathbf{R}_A$, we can use $\mathbf{b}_0 = -(\mathbf{a}_1 + \mathbf{a}_2)/3$ and write $\boldsymbol{\mathcal{R}}_A(p,q) = \boldsymbol{\mathcal{R}}(p - 1/3, q - 1/3)$. By using the reversed transformation in Eq. (27), the position vector $\boldsymbol{\mathcal{R}}_A(r,s) = \boldsymbol{\mathcal{R}}(r - (m-n)/(3D), s - d(h_1 - h_2)/(3D))$ is then found. Finally, we map $\boldsymbol{\mathcal{R}}_A(r,s)$ to $\mathbf{R}_A(r,s)$ by Eq. (29), and then the coordinate of each lattice point is found.

D. Helical band structure

Since the unrolled coordinate $\boldsymbol{\mathcal{R}}$ and the rolled-up coordinate $\mathbf{R}$ have one-to-one correspondence, the tight-binding Hamiltonian for an SWNT with the uniform magnetic-field interaction can be rewritten in the unrolled coordinate as

$$\begin{aligned}\hat{\mathcal{H}}_{\mathrm{TB}} &= -t \sum_{\boldsymbol{\mathcal{R}}\alpha} \sum_{\sigma=\{0,1,2\}} \exp(\mathrm{i}\chi_\sigma)\hat{a}^\dagger_{\boldsymbol{\mathcal{R}}+\mathbf{b}_\sigma-\mathbf{b}_0,A\alpha}\hat{a}_{\boldsymbol{\mathcal{R}}B\alpha} \\ &\quad - t' \sum_{\boldsymbol{\mathcal{R}}\mu\alpha} \sum_{\varsigma=\{1,2,3\}} \exp(\mathrm{i}\chi'_\varsigma)\hat{a}^\dagger_{\boldsymbol{\mathcal{R}}+\mathbf{a}_\varsigma,\mu\alpha}\hat{a}_{\boldsymbol{\mathcal{R}}\mu\alpha} \\ &\quad + \mathrm{H.c.}, \end{aligned} \tag{35}$$

where χ_σ and χ'_ς are the Peierls phase factors, $\mathbf{b}_0 = -(\mathbf{a}_1 + \mathbf{a}_2)/3$, $\mathbf{b}_1 = \mathbf{b}_0 + \mathbf{a}_1$, $\mathbf{b}_2 = \mathbf{b}_0 + \mathbf{a}_2$ are the vectors pointing to

the three nearest-neighbor sites, and $\pm\mathbf{a}_1, \pm\mathbf{a}_2, \pm\mathbf{a}_3 = \pm(\mathbf{a}_1 - \mathbf{a}_2)$ are the vectors pointing to the six next-nearest-neighbor sites. By the coordinate transformation in Eq. (27), the lattice vectors based on helical-rotational construction are

$$\mathbf{a}_1 = \frac{m}{D}\boldsymbol{\tau}_1 - \frac{dh_2}{D}\boldsymbol{\tau}_2, \quad \mathbf{a}_2 = -\frac{n}{D}\boldsymbol{\tau}_1 + \frac{dh_1}{D}\boldsymbol{\tau}_2. \tag{36}$$

On the derivation of the Peierls phase factor under an axial magnetic field, we can take advantage of that

$$\mathbf{e}_3 \cdot (\mathbf{R}_{1\mu} \times \mathbf{R}_{2\nu}) = -\rho_0^2 \sin[(\boldsymbol{\mathcal{R}}_{1\mu} - \boldsymbol{\mathcal{R}}_{2\nu}) \cdot \boldsymbol{\phi}]. \tag{37}$$

With the axial magnetic field $\boldsymbol{\mathcal{B}} = \mathcal{B}\mathbf{e}_3$, the phase factors become $\chi_\sigma = (e\rho_0^2\mathcal{B}/2)\sin(\mathbf{b}_\sigma \cdot \boldsymbol{\phi})$, and $\chi'_\varsigma = (e\rho_0^2\mathcal{B}/2)\sin(\mathbf{a}_\varsigma \cdot \boldsymbol{\phi})$. While the phase factors are independent of $\mathbf{R}$, which contains the local geometrical information, the axial magnetic field only contributes a global phase shift which is proportional to the cross section of the nanotube $\pi\rho_0^2$ to the hopping couplings. It is a feature of Aharonov-Bohm effect that the phase shift is nonlocal [36].

With the periodic boundary conditions $\mathbf{R}(r+N,s) = \mathbf{R}(r,s)$ and $\mathbf{R}(r,s+d) = \mathbf{R}(r,s)$, the Fermi operator can be transformed into the reciprocal space of the lattice vectors based on the helical-rotational construction by the discrete Fourier transform

$$\hat{a}_{\boldsymbol{\mathcal{R}}\mu\alpha} = \frac{1}{\sqrt{\mathcal{N}}}\sum_{\mathbf{k}} e^{i\mathbf{k}\cdot\boldsymbol{\mathcal{R}}_\mu}\hat{a}_{\mathbf{k}\mu\alpha}, \tag{38}$$

$$\hat{a}^\dagger_{\boldsymbol{\mathcal{R}}\mu\alpha} = \frac{1}{\sqrt{\mathcal{N}}}\sum_{\mathbf{k}} e^{-i\mathbf{k}\cdot\boldsymbol{\mathcal{R}}_\mu}\hat{a}^\dagger_{\mathbf{k}\mu\alpha}, \tag{39}$$

where the wave vector is given by

$$\mathbf{k} = \frac{\kappa}{2\pi}\mathbf{g}_1 + \frac{\lambda}{d}\mathbf{g}_2, \tag{40}$$

with $\kappa = 2\pi K/N$ with $K = 0,1,\ldots,N-1$ the helical momentum and $\lambda = 0,\ldots,d-1$ the circumferential angular momentum, and $\mathcal{N} = Nd$ is the total number of lattice points. Then the tight-binding Hamiltonian can be rewritten as

$$\hat{\mathcal{H}}_{\rm TB} = \sum_{\mu\nu,\alpha}\sum_{\mathbf{k}} h_{\mathbf{k},\mu\nu}\hat{a}^\dagger_{\mathbf{k}\mu\alpha}\hat{a}_{\mathbf{k}\nu\alpha}, \tag{41}$$

where $h_{\mathbf{k},\mu\nu}$ is the single-particle Hamiltonian matrix in k space and the matrix elements are

$$h_{\mathbf{k},AA} = h_{\mathbf{k},BB} = -2t' \sum_{\varsigma=\{1,2,3\}} \cos(\mathbf{k}\cdot\mathbf{a}_\varsigma - \chi'_\varsigma), \tag{42}$$

$$h_{\mathbf{k},AB} = h^*_{\mathbf{k},BA} = -t \sum_{\sigma=\{0,1,2\}} \exp(-\mathrm{i}\mathbf{k}\cdot\mathbf{b}_\sigma + \mathrm{i}\chi_\sigma). \tag{43}$$

It is found that the next-nearest-neighbor hopping coupling contributes equivalently to the diagonal term of the Hamiltonian matrix. This term can be seen as a sinusoidal function added to the band structure, and it breaks the electron-hole symmetry.

By an unitary transformation of the creation and annihilation operators into crystal-orbital basis,

$$\hat{a}_{\mathbf{k}\mu\alpha} = \sum_i u_{\mathbf{k}i,\mu}\hat{c}_{\mathbf{k}i\alpha}, \ \hat{a}^\dagger_{\mathbf{k}\mu\alpha} = \sum_i u^*_{\mathbf{k}i,\mu}\hat{c}^\dagger_{\mathbf{k}i\alpha}, \tag{44}$$

where $u_{\mathbf{k}i,\mu}$ is called crystal-orbital coefficient, the tight-binding Hamiltonian in the basis becomes

$$\hat{\mathcal{H}}_{\rm TB} = \sum_{i\alpha}\sum_{\mathbf{k}} \varepsilon_{\mathbf{k}i}\hat{c}^\dagger_{\mathbf{k}i\alpha}\hat{c}_{\mathbf{k}i\alpha}. \tag{45}$$

The energy band $\varepsilon_{\mathbf{k}i}$ and the transformation parameter $u_{\mu i}(\mathbf{k})$ can be obtained by solving the secular equation

$$\underline{h}_{\mathbf{k}}\underline{u}_{\mathbf{k}i} = \varepsilon_{\mathbf{k}i}\underline{u}_{\mathbf{k}i}, \tag{46}$$

where the underline indicates that the symbol is a matrix or column vector. The band energy is given by

$$\varepsilon_{\mathbf{k}\pm} = h_{\mathbf{k},AA} \pm t\sqrt{3 + 2(\cos\theta_{\mathbf{k}1} + \cos\theta_{\mathbf{k}2}) + 2\cos(\theta_{\mathbf{k}1} - \theta_{\mathbf{k}2})}, \tag{47}$$

where $\theta_{\mathbf{k}1} = (\kappa m - 2\pi\lambda h_2)/D - \chi_1 + \chi_0$ and $\theta_{\mathbf{k}2} = -(\kappa n - 2\pi\lambda h_1)/D - \chi_2 + \chi_0$. The condition of the zero band gap is $\theta_{\mathbf{k}1} = -\theta_{\mathbf{k}2} = \pm 2\pi/3$. The condition can be fulfilled only if the circumferential angular momentum is given by

$$\lambda = \pm\frac{n-m}{3} + \frac{n(\chi_1 - \chi_0) - m(\chi_2 - \chi_0)}{2\pi}. \tag{48}$$

Since λ is an integer, the metallicity condition that $|n-m|$ is divided by three can be found without the axial magnetic field. The axial magnetic field might play the role to open or shrink the band gap of a SWNT.

Similar helical band structures of SWNTs under an axial magnetic field had been derived by Lu [37]. However, there is a subtle difference between Lu's formula and Eq. (47). In Lu's derivation, the integration in Peierls phase factor is calculated by pure geometrical argument, instead of using designated atomic position as in the present paper. Even though the two derivations have the difference, the qualitative results are basically the same.

Figures 2(a), 2(b), and 2(c) are the three examples of helical band structures and their corresponding density of state. Different to conventional band structures of SWNTs, the helical band structures are indexed by the helical momentum κ, and the circumferential-angular momentum λ can be identified as shown in the figure. One thing worth noting is that the $\lambda = 0$ band of (6,4)−SWNT is completely identical to the $\lambda = 0$ band of (9,6)−SWNT under tight-binding approximation. Actually, it is not difficult to show by Eq. (47) that the SWNTs whose chiral indices have the same factor-number pair, in our case (3,2) for (6,4) and (9,6), have at least one identical helical band. Therefore, it also can be shown that the $\lambda = 0$ band in both SWNTs is identical to the helical band of (3,2)−SWNT. Under an extremely large axial magnetic field of 3000 Tesla, as shown as the dot lines in Fig. 2, the helical band structures show helical-momentum dependent and circumferential-angular-momentum dependent variations, which cause band gap opening or closing. The clear dependence makes the helical band structure a good tool to analyze the single-electron properties of SWNTs.

E. Matrix elements and selection rules

To simplify the derivation, we transform the coordinate system by the Jones vectors

$$\mathbf{e}_+ = \mathbf{e}_1 + \mathrm{i}\mathbf{e}_2, \quad \mathbf{e}_- = \mathbf{e}_1 - \mathrm{i}\mathbf{e}_2, \tag{49}$$

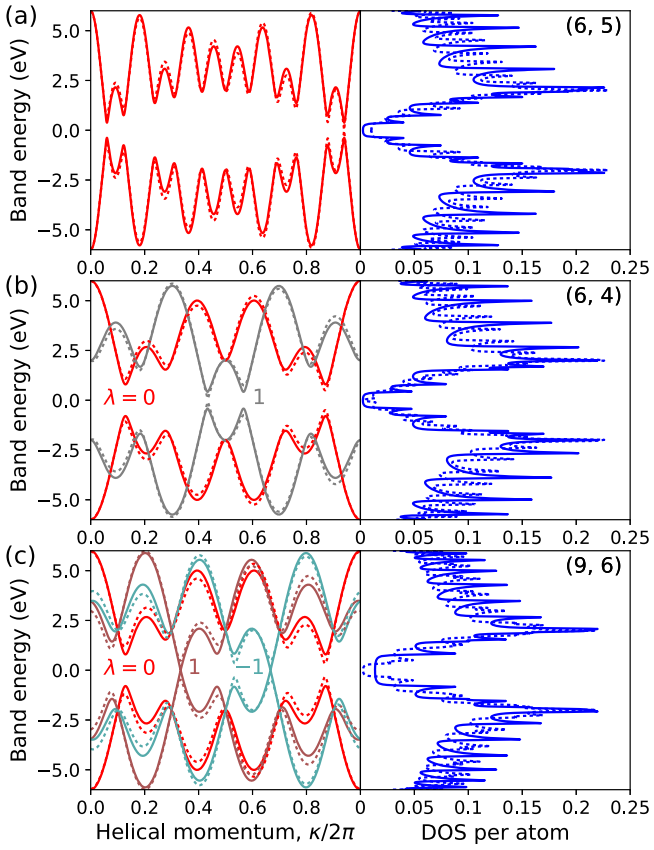

FIG. 2. Helical band structure and density of state of (a) (6,5)−SWNT with $\phi_{\rm H}/(2\pi) = -0.18$, (b) (6,4)−SWNT with $\phi_{\rm H}/(2\pi) = 0.30$, and (c) (9,6)−SWNT with $\phi_{\rm H}/(2\pi) = 0.20$ calculated by the tight-binding approximation with the hopping couplings are $t = 2$ eV and $t' = 0$ eV without (solid line) and with (dash line) an axial magnetic field of 3000 Tesla.

which correspond to the right-handed and left-handed circular polarization vectors, with $\mathbf{e}_3$ remaining a basis. The position vector is then separated as axial part ($R^{\parallel}$) and circumferential part ($R^{\pm}$) as

$$\mathbf{R} = R^{+}\mathbf{e}_{+} + R^{-}\mathbf{e}_{-} + R^{\parallel}\mathbf{e}_3, \tag{50}$$

$$R^{\parallel}(r,s) = r z_{\rm H}, \;\; R^{\pm}(r,s) = \frac{\rho_0}{2}\mathrm{e}^{\mp \mathrm{i}\mathcal{R}\cdot\boldsymbol{\phi}}. \tag{51}$$

The electric dipole-moment operator and magnetic-moment operator can also be decomposed by a linear combination of the axial part ($\hat{\mu}^{\parallel}$, $\hat{m}^{\parallel}$) and circumferential part ($\hat{\mu}^{\pm}$, $\hat{m}^{\pm}$). The axial dipole-moment operator can be expressed as

$$\begin{aligned}\hat{\mu}^{\parallel} &= \frac{e}{\mathcal{N}}\sum_{\mathcal{R}\mu,\alpha}\sum_{\mathbf{kq}}(\mathrm{e}^{-\mathrm{i}\mathbf{q}\cdot\mathcal{R}_\mu}R^{\parallel}_{\mu})\hat{a}^{\dagger}_{\mathbf{k}\mu\alpha}\hat{a}_{\mathbf{k}-\mathbf{q},\mu\alpha}\\ &= e\sum_{\mathbf{k}\mu,\alpha}\hat{a}^{\dagger}_{\mathbf{k}\mu\alpha}(\mathrm{i}\nabla^{\parallel}_{\mathbf{k}})\hat{a}_{\mathbf{k}\nu\alpha}\\ &= e\sum_{ij,\alpha}\sum_{\mathbf{k}}[\xi^{\parallel}_{\mathbf{k}ij}\hat{c}^{\dagger}_{\mathbf{k}i\alpha}\hat{c}_{\mathbf{k}j\alpha} + \delta_{ij}\hat{c}^{\dagger}_{\mathbf{k}i\alpha}(\mathrm{i}\nabla^{\parallel}_{\mathbf{k}})\hat{c}_{\mathbf{k}i\alpha}],\end{aligned} \tag{52}$$

where $\xi^{\parallel}_{\mathbf{k}ij} = \mathrm{i}\underline{u}^{\dagger}_{\mathbf{k}i}\nabla^{\parallel}_{\mathbf{k}}\underline{u}_{\mathbf{k}j}$ is the axial dipole-moment matrix element, and $\nabla^{\parallel}_{\mathbf{k}} = z_{\rm H}(\partial/\partial\kappa)$. In the derivation of the second line in Eq. (52), we have used $\mathrm{i}\nabla^{\parallel}_{\mathbf{q}}(\mathrm{e}^{-\mathrm{i}\mathbf{q}\cdot\mathcal{R}_\mu}) = \mathrm{e}^{-\mathrm{i}\mathbf{q}\cdot\mathcal{R}_\mu}R^{\parallel}_{\mu}$ and $(1/\mathcal{N})\sum_{\mathcal{R}}\mathrm{e}^{-\mathrm{i}\mathbf{q}\cdot\mathcal{R}_\mu} = \delta_{\mathbf{q0}}$. In the continuous limit with the summation replaced by integration, $\sum_{\mathbf{q}} \to \int \frac{\mathrm{d}\mathbf{q}}{2\pi}$, and the Kronecker's delta by the Dirac delta, $\delta_{\mathbf{q0}} \to 2\pi\delta(\mathbf{q})$, we can obtain

$$\begin{aligned}&\sum_{\mathbf{q}}(\nabla^{\parallel}_{\mathbf{q}}\delta_{\mathbf{q0}})\hat{a}^{\dagger}_{\mathbf{k}\mu\alpha}\hat{a}_{\mathbf{k}-\mathbf{q},\mu\alpha} \to -\int \mathrm{d}\mathbf{q}\delta(\mathbf{q})\hat{a}^{\dagger}_{\mathbf{k}\mu\alpha}\nabla^{\parallel}_{\mathbf{q}}\hat{a}_{\mathbf{k}-\mathbf{q},\mu\alpha}\\ &= \int \mathrm{d}\mathbf{q}\delta(\mathbf{q})\hat{a}^{\dagger}_{\mathbf{k}\mu\alpha}\nabla^{\parallel}_{\mathbf{k}}\hat{a}_{\mathbf{k}-\mathbf{q},\mu\alpha}\\ &= \hat{a}^{\dagger}_{\mathbf{k}\mu\alpha}\nabla^{\parallel}_{\mathbf{k}}\hat{a}_{\mathbf{k}\mu\alpha}\end{aligned} \tag{53}$$

by the integration by parts. The second line of the derivation is merely a change of variable. These techniques are applied repeatedly in the derivations of matrix elements. The first term in the last line in Eq. (52) corresponds to the electron-hole excitation, while the second term stands for the electron or hole transport. Note that, for standard linear spectra, only the first term contributes to the transition amplitude. The selection rule for the parallel-polarized transition is thus given by

$$\Delta\kappa = \Delta\lambda = 0, \tag{54}$$

which is also the selection rule of vertical transition. It is also straightforward to derive the circumferential dipole-moment operator

$$\begin{aligned}\hat{\mu}^{\pm} &= \frac{e}{\mathcal{N}}\sum_{\mathcal{R}\mu,\alpha}\sum_{\mathbf{kq}}(\mathrm{e}^{-\mathrm{i}\mathbf{q}\cdot\mathcal{R}_\mu}R^{\pm}_{\mu})\hat{a}^{\dagger}_{\mathbf{k}\mu\alpha}\hat{a}_{\mathbf{k}-\mathbf{q},\mu\alpha}\\ &= e\sum_{ij,\alpha}\sum_{\mathbf{k}}\xi^{\pm}_{\mathbf{k}ij}\hat{c}^{\dagger}_{\mathbf{k}\mp\boldsymbol{\phi},i\alpha}\hat{c}_{\mathbf{k}j\alpha},\end{aligned} \tag{55}$$

where $\xi^{\pm}_{\mathbf{k}ij} = (\rho_0/2)\underline{u}^{\dagger}_{\mathbf{k}\mp\boldsymbol{\phi},i}\underline{u}_{\mathbf{k}j}$ is the circumferential dipole-moment matrix element. The corresponding selection rules for the cross-polarized transition are found

$$\Delta\kappa = \pm\phi_{\rm H}, \quad \Delta\lambda = \pm\frac{d}{2\pi}\phi_{\rm R} = \pm 1. \tag{56}$$

The selection rules reflect the intrinsic helical-rotational symmetry of the SWNTs and the momentum transfer of the optical transitions. Based on the coordinate system, the selection rules with two opposite signs can be assigned as left-handed circularly-polarized transition ($\Delta\kappa = \phi_{\rm H}$, $\Delta\lambda = 1$) and right-handed circularly-polarized transition ($\Delta\kappa = -\phi_{\rm H}$, $\Delta\lambda = -1$).

The axial magnetic-moment operator can be found by using Eq. (15) and Eq. (37) as

$$\begin{aligned}\hat{m}^{\parallel} &= \mathrm{i}\frac{et\rho_0^2}{2}\mathbf{e}_3\sum_{\mathbf{k}\alpha,\sigma}\sin(\mathbf{b}_\sigma\cdot\boldsymbol{\phi})\mathrm{e}^{-\mathrm{i}\mathbf{k}\cdot\mathbf{b}_\sigma+\mathrm{i}\chi_\sigma}\hat{a}^{\dagger}_{\mathbf{k}A\alpha}\hat{a}_{\mathbf{k}B\alpha}\\ &\quad - \mathrm{i}\frac{et'\rho_0^2}{2}\mathbf{e}_3\sum_{\mathbf{k}\mu\alpha,\varsigma}\sin(\mathbf{a}_\varsigma\cdot\boldsymbol{\phi})\mathrm{e}^{-\mathrm{i}\mathbf{k}\cdot\mathbf{a}_\varsigma+\mathrm{i}\chi'_\varsigma}\hat{a}^{\dagger}_{\mathbf{k}\mu\alpha}\hat{a}_{\mathbf{k}\mu\alpha} + \mathrm{H.c.}\\ &= e\sum_{ij,\alpha}\sum_{\mathbf{k}}l^{\parallel}_{\mathbf{k}ij}\hat{c}^{\dagger}_{\mathbf{k}i\alpha}\hat{c}_{\mathbf{k}j\alpha},\end{aligned} \tag{57}$$

where $l^{\parallel}_{\mathbf{k}ij} = (\rho_0^2/4)\underline{u}^{\dagger}_{\mathbf{k}i}(\underline{h}_{\mathbf{k}+\boldsymbol{\phi}} - \underline{h}_{\mathbf{k}-\boldsymbol{\phi}})\underline{u}_{\mathbf{k}j}$ is the magnetic-moment matrix element. Finally, after some straightforward

algebra, the circumferential magnetic-moment operator is derived as

$$\begin{aligned}\hat{m}^{\pm} = & e\sum_{ij,\alpha}\sum_{\mathbf{k}} l^{\pm}_{\mathbf{k}ij}\hat{c}^{\dagger}_{\mathbf{k}\mp\boldsymbol{\phi},i\alpha}\hat{c}_{\mathbf{k}j\alpha} \\ & + e\sum_{ij,\alpha}\sum_{\mathbf{k}}\left[\pi^{\pm}_{\mathbf{k}ij}\left(\nabla^{\parallel}_{\mathbf{k}\mp\boldsymbol{\phi}}\hat{c}^{\dagger}_{\mathbf{k}\mp\boldsymbol{\phi},i\alpha}\right)\hat{c}_{\mathbf{k}j\alpha}\right. \\ & \left. + \tilde{\pi}^{\pm}_{\mathbf{k}ij}\hat{c}^{\dagger}_{\mathbf{k}\mp\boldsymbol{\phi},i\alpha}\left(\nabla^{\parallel}_{\mathbf{k}}\hat{c}_{\mathbf{k},j\alpha}\right)\right], \end{aligned} \tag{58}$$

where

$$\begin{aligned} l^{\pm}_{\mathbf{k}ij} = & \mp\mathrm{i}\frac{\rho_0}{4}\left[\left(\nabla^{\parallel}_{\mathbf{k}\mp\boldsymbol{\phi}}\underline{u}^{\dagger}_{\mathbf{k}\mp\boldsymbol{\phi},i}\right)\underline{h}_{\mathbf{k}\mp\boldsymbol{\phi}}\underline{u}_{\mathbf{k}j}\right. \\ & \left. + \underline{u}^{\dagger}_{\mathbf{k}\mp\boldsymbol{\phi},i}\underline{h}_{\mathbf{k}}\left(\nabla^{\parallel}_{\mathbf{k}}\underline{u}_{\mathbf{k}j}\right)\right], \end{aligned} \tag{59}$$

$$\pi^{\pm}_{\mathbf{k}ij} = \mp\mathrm{i}\frac{\rho_0}{4}\underline{u}^{\dagger}_{\mathbf{k}\mp\boldsymbol{\phi},i}\underline{h}_{\mathbf{k}\mp\boldsymbol{\phi}}\underline{u}_{\mathbf{k}j}, \tag{60}$$

$$\tilde{\pi}^{\pm}_{\mathbf{k}ij} = \mp\mathrm{i}\frac{\rho_0}{4}\underline{u}^{\dagger}_{\mathbf{k}\mp\boldsymbol{\phi},i}\underline{h}_{\mathbf{k}}\underline{u}_{\mathbf{k}j}. \tag{61}$$

Again, as in the case of axial dipole-moment operator, only the first term of the circumferential magnetic-moment operator contributes to linear spectra. Examining these operators, it is apparent that the selection rules of the polarized transitions in the CD spectrum are the same as the ones in the absorption spectrum.

F. Coulomb interaction and exciton calculation

In the presence of the Coulomb interaction among electrons, the band energies and crystal orbital coefficients are altered. In the present paper, the ground-state wave function is approximated by the Hartree-Fock configuration $|\Psi_{\mathrm{HF}}\rangle$, and the band energies and the crystal orbital coefficients are solved by the Hartree-Fock equation [75]

$$\underline{F}_{\mathbf{k}}\underline{u}_{\mathbf{k}i} = \varepsilon_{\mathbf{k}i}\underline{u}_{\mathbf{k}i}. \tag{62}$$

The Fock matrix is written by

$$\begin{aligned} F_{\mathbf{k},\mu\nu} = & h_{\mathbf{k},\mu\nu} - \frac{1}{\mathcal{N}}\sum_{\mathbf{q}} p_{\mathbf{k}-\mathbf{q},\mu\nu}V_{\mathbf{q},\mu\nu} \\ & + \delta_{\mu\nu}\left(w_{\mu} + \frac{2}{\mathcal{N}}\sum_{\mathbf{q}}\sum_{\lambda} V_{\mathbf{0},\mu\lambda}p_{\mathbf{k}-\mathbf{q},\lambda\lambda}\right), \end{aligned} \tag{63}$$

with $w_{\mu} = -U/2 - \sum_{\nu} V_{\mathbf{0},\mu\nu}$, and the Coulomb-integral matrix is

$$\begin{aligned} V_{\mathbf{q},\mu\nu} = & \delta_{\mu\nu}U + \sum_{\boldsymbol{\mathcal{R}}_{1\mu}-\boldsymbol{\mathcal{R}}_{2\nu}(\neq 0)} \mathrm{e}^{-\mathrm{i}\mathbf{q}\cdot(\boldsymbol{\mathcal{R}}_{1\mu}-\boldsymbol{\mathcal{R}}_{2\nu})} \\ & \times \frac{e^2}{\epsilon_{\mathrm{r}}\sqrt{(e^2/U)^2 + |\mathbf{R}_{1\mu}-\mathbf{R}_{2\nu}|^2}}. \end{aligned} \tag{64}$$

The single-particle density matrix is given by $\underline{p}_{\mathbf{k}} = \underline{u}_{\mathbf{k}v}\underline{u}^{\dagger}_{\mathbf{k}v}$, with v indicating valence band. As convention, a self-consistent field calculation is supposed to be designed to solve the Hartree-Fock equation.

The excited state is approximated by a superposition of the singly-excited configuration state functions [76],

$$|\Phi_M\rangle = \sum_{\mathbf{kq}} C_{\mathbf{k}cv,M}(\mathbf{q})\frac{1}{\sqrt{2}}\left[\hat{c}^{\dagger}_{\mathbf{k}+\mathbf{q},c\uparrow}\hat{c}_{\mathbf{k}v\uparrow} + \hat{c}^{\dagger}_{\mathbf{k}+\mathbf{q},c\downarrow}\hat{c}_{\mathbf{k}v\downarrow}\right]|\Psi_{\mathrm{HF}}\rangle, \tag{65}$$

where subscripts c and v denote conduction and valence bands, respectively. The excitation energy can be calculated by the eigenvalue problem,

$$\underline{\Omega}(\mathbf{q})\underline{C}_M(\mathbf{q}) = \omega_M(\mathbf{q})\underline{C}_M(\mathbf{q}), \tag{66}$$

where $\omega_M(\mathbf{q})$ is the Mth excitation energy. The excitation matrix is given by

$$\Omega_{\mathbf{k}cv;\mathbf{k}'cv}(\mathbf{q}) = \delta_{\mathbf{k}\mathbf{k}'}(\varepsilon_{\mathbf{k}+\mathbf{q},c} - \varepsilon_{\mathbf{k}v}) + \frac{1}{\mathcal{N}}\mathcal{K}_{\mathbf{k}cv;\mathbf{k}'cv}(\mathbf{q}), \tag{67}$$

where the kernel matrix is

$$\begin{aligned} \mathcal{K}_{\mathbf{k}ij;\mathbf{k}'i'j'}(\mathbf{q}) = & \sum_{\mu\nu}\left[2u^{*}_{\mathbf{k}+\mathbf{q}i,\mu}u_{\mathbf{k}j,\mu}u_{\mathbf{k}'+\mathbf{q}i',\nu}u^{*}_{\mathbf{k}'j',\nu}V_{\mathbf{q},\mu\nu}\right. \\ & \left. - u^{*}_{\mathbf{k}+\mathbf{q}i,\mu}u_{\mathbf{k}'+\mathbf{q}i',\mu}u_{\mathbf{k}j,\nu}u^{*}_{\mathbf{k}'j',\nu}V_{\mathbf{k}-\mathbf{k}',\mu\nu}\right]. \end{aligned} \tag{68}$$

The first term of the kernel matrix is known as exchange interaction and the second term is known as direct Coulomb interaction. With the selection rules given in Sec. II E, we only need to diagonalize the excitation matrix with $\mathbf{q} = \mathbf{0}, \pm\boldsymbol{\phi}$.

To simulate the optical spectra, we need to know how to solve the axial dipole-moment matrix element $\xi^{\parallel}_{\mathbf{k}ij}$ and circumferential magnetic-moment matrix element $l^{\pm}_{\mathbf{k}ij}$ under Hartree-Fock approximation. The computation involves the derivative of the crystal orbital coefficient $\nabla^{\parallel}_{\mathbf{k}}\underline{u}_{\mathbf{k}j}$. With the Hartree-Fock self-consistent field potential, the derivative of the crystal orbital coefficient is supposed to be solved by coupled-perturbed Hartree-Fock equations [75] (also see the Supplemental Material [74]).

A numerical issue needs to be addressed. Since the single-particle Hamiltonian matrix gives the periodic conditions $\underline{h}_{\mathbf{k}+\mathbf{g}_1} = e^{\mathrm{i}2\pi(m-n)/(3d)}\underline{h}_{\mathbf{k}}$ and $\underline{h}_{\mathbf{k}+\mathbf{g}_2} = e^{\mathrm{i}2\pi(h_1-h_2)/3}\underline{h}_{\mathbf{k}}$, the Fock matrix, Coulomb-integral matrix, and the crystal-orbital coefficient should have the same periodicity with respect to the helical momentum and the quasiangular momentum. In numerical calculation, the phase term could be cumbersome to deal. An alternative formulation which can eliminate the phase term is to replace the discrete Fourier transform in Eq. (38) by $\hat{a}_{\boldsymbol{\mathcal{R}}\mu\alpha} = (1/\sqrt{\mathcal{N}})\sum_{\mathbf{k}} \mathrm{e}^{i\mathbf{k}\cdot\boldsymbol{\mathcal{R}}}\hat{a}_{\mathbf{k}\mu\alpha}$. Note the $\boldsymbol{\mathcal{R}}_{\mu}$ in Eq. (38) is replaced by $\boldsymbol{\mathcal{R}}$. By the formulation, the matrix elements are needed to rewrite as more complicated forms, but the implementation is more straightforward.

III. RESULTS AND DISCUSSIONS

In the present paper, we have performed the simulations on the optical absorption and the CD of chiral SWNTs with different chiral indices by the PPP Hamiltonian. The parameters $t = 2.0$ eV, $t' = 0.4$ eV, $U = 11.0$ eV, and $\epsilon_{\mathrm{r}} = 2.8$ are chosen, except in Fig. 4 that the next-nearest-neighbor hopping coupling t' is varied to discuss its effect. $\mathcal{N} = 3600$ unit cells are used to generate the discrete $\mathbf{k}$ space for each

TABLE I. d_0: diameter (Å); E_b: exciton binding energy (eV); E_{11} and E_{22}: the transition energies (eV) of the first and second bright-exciton states; f_{11}: oscillator strength per atom of the first exciton state.

index	d_0	E_b^{cal}	E_{11}^{cal}	f_{11}^{cal}	E_{22}^{cal}	E_b^{exp}	E_{11}^{exp}	f_{11}^{exp}	E_{22}^{exp}
(6,4)	6.83	0.50	1.33	0.069	2.27		1.42[b]	0.027[c]	2.13[b]
(6,5)	7.47	0.46	1.23	0.063	2.15	0.43[a]	1.27[b]	0.029[c]	2.19[b]
(7,5)	8.17	0.43	1.14	0.058	1.96	0.39[a]	1.21[b]	0.016[c]	1.93[b]
(8,4)	8.29	0.41	1.12	0.058	2.00		1.11[b]		2.11[b]
(9,6)	10.24	0.54	2.36	0.080	4.13		2.24[d]		

[a]From Ref. [9].
[b]From Ref. [6].
[c]From Ref. [10].
[d]From Ref. [8].

calculation, except $\mathcal{N} = 6000$ unit cells are used in Fig. 7 for ensuring convergence. The spectral line shape in each figure is described by Lorentz's function and the integration over each Lorentz's function gives the corresponding oscillator/rotation strength per atom of the transition. The strengths of CD spectra given by Eq. (22) are rescaled by multiplying a factor of c_0 for comparison.

Table I shows the calculated exciton binding energies, transition energies, oscillator strengths of the first parallel-polarized exciton (E_{11}) and the transition energies of the second parallel-polarized exciton (E_{22}), and the corresponding experimental values from the literatures. As can be seen in the table, the optical properties except the oscillator strength of the SWNTs with different chiral indices can be described well with the present model and parameters. The large discrepancy in oscillator strength, however, is expected [69] since we use the singly-excited configuration interaction method as the variational exciton wave function. This method is known to overestimate the oscillator strength up to two- to threefold due to lack of including the effect of multiexciton excitation. In some molecular scale simulations, an inclusion of doubly-excited configuration interaction wave function can circumvent the discrepancy largely. Besides, ignoring the contribution of σ-electron polarization to optical transition by PPP Hamiltonian is also a reason of overestimating oscillator strength [69]. In the present study, we will not go further to discuss the discrepancy and the correction since they are beyond the scope. As a *ad hoc* approach, the discrepancy can always be reduced by empirically scaling the charge coupling strength $|e|^2$ by a factor, only that we are not doing here.

A. Exciton spectra of (6,5)−SWNT

While we apply both the exciton calculation and helical-rotational symmetry to the study of polarized excitons and optical activity in SWNTs, a detailed comparison of the calculated spectra with the experimental ones might be helpful to realize the utility and limitation of the present formalism. In this section, we focus on the exciton spectra of (6,5)−SWNT, since (6,5)−SWNT is a commonly used model isomer in both theoretical and experimental studies. In the next section, calculated results of several SWNTs with different chiral indices are provided.

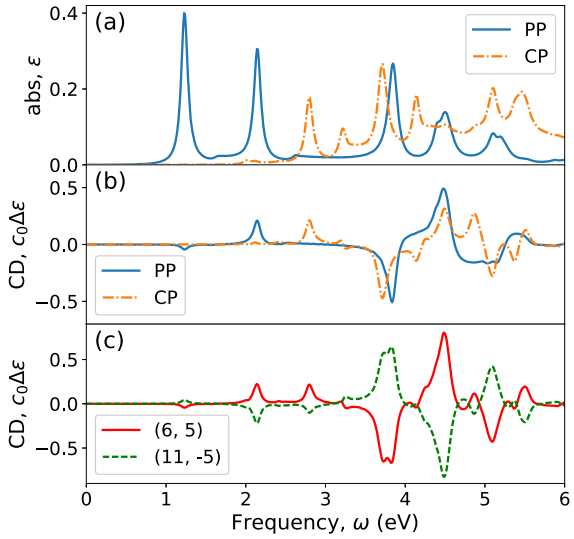

FIG. 3. Calculated parallel-polarized (PP) and cross-polarized (CP) transitions in (a) absorption and (b) CD spectra of (6,5)−SWNT. In (c), the CD spectra of (6,5)−SWNT and the corresponding enantiomer (11,−5)−SWNT with the combination of parallel-polarized and cross-polarized transitions are displayed and compared. The linewidth is 0.05 eV.

In Figs. 3(a) and 3(b), the calculated parallel-polarized and cross-polarized transitions in absorption and CD spectra of (6,5)−SWNT are shown. As shown in the figure, the parallel-polarized transitions in the absorption spectrum show apparent excitonic characters and well matching with the reported experimental spectrum [26,27]. For the first four excitonic transitions, assigned as E_{11} to E_{44}, the positions of the peaks and the relative order in oscillator strengths are well described except that the excitation energies of the third and forth excitonic transitions are overestimated about 0.25 eV. The result is acceptable since both the model Hamiltonian and the methodology are quite simple. Besides the absorption spectrum, the calculated CD is also well comparable, while the basic features of the excitonic transitions match roughly with the assigned transitions from the reports [26,27].

For the cross-polarized transitions in Fig. 3(a), the calculated absorption spectrum shows unfamiliar feature for the regime that the frequency is higher than the second excitonic transition. Spectral peaks which are not observed or obscure in the experimental spectra show strong oscillator strengths [26,27]. The obscurity of the strong transition in the experimental spectra can be explained by depolarization effect. As proposed by Ajiki [36], Ando and Uryu [31], the cross-polarized excitons are susceptible to the depolarization effect, which is induced by a depolarization field between plus and minus charges generated by the light electric field polarized perpendicularly to the tube axis. This effect causes two results. First, the Tamm-Dancoff-type approximation, which is the singly-excited configuration interaction in the present case, is no longer enough to describe cross-polarized excitons. A self-consistent-field calculation to include the depolarization field is supposed to be applied [34]. Second, the cross-polarized excitons might be sensitive to the surrounding materials such as surfactants and solvents. A more sophisticated dielectric

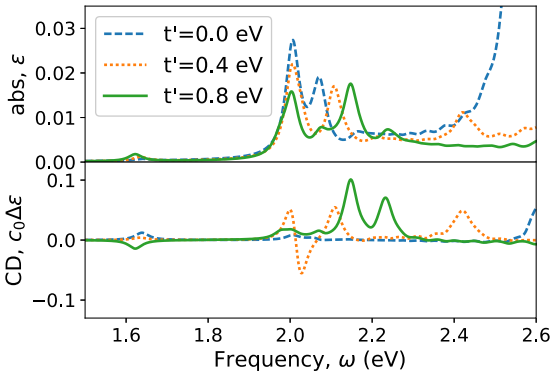

FIG. 4. Calculated cross-polarized transitions in absorption (up) and CD (down) spectra of (6,5)−SWNT with different next-nearest-neighbor hopping couplings. The linewidth is 0.02 eV.

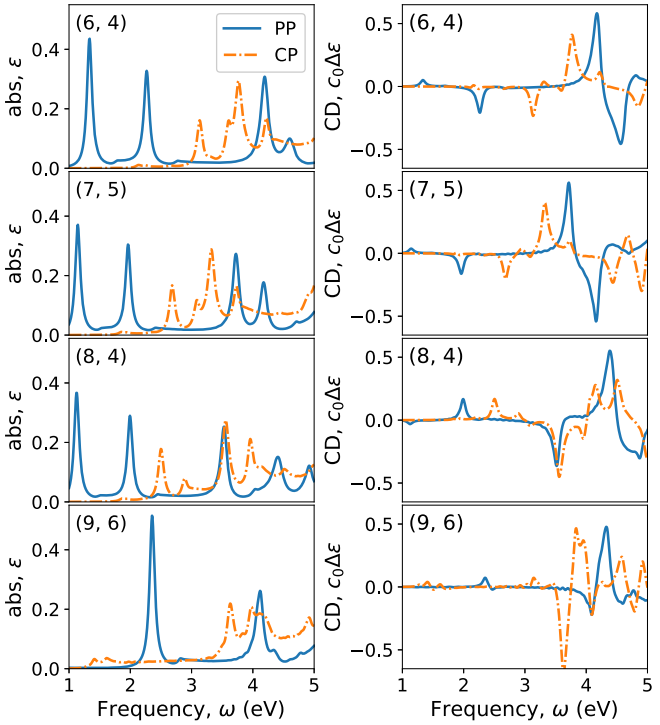

FIG. 5. Calculated absorption (left) and CD (right) spectra of SWNTs with different chiral indices. The solid lines are the parallel-polarized (PP) transitions and the dash lines are the cross-polarized (CP) transitions. The linewidth is 0.05 eV.

screening function might be needed to be designed [35]. While the present study does not fully consider the two factors, the overestimation of the strengths of cross-polarized transitions is unavoidable.

Because the strengths of the low-energy cross-polarized transitions are weak in comparison with the whole spectrum in Fig. 3, a rescaled diagram for the low-energy transitions with narrower spectral linewidth are drawn as the dot-line in Fig. 4. The calculated lowest two cross-polarized transitions are at 1.63 eV with barely observable strength and at 2.00 eV with observable strength. Although normally the lowest-energy peak is assigned as the experimentally reported $E_{12}^{\text{exp}} = 1.90$ eV transition [30], we suspect that the second one might be more suitable to be assigned as the observed transition. The relative strength between the two transitions is one reason. Another reason can be referred to the corresponding rotatory transitions in the CD spectrum in Fig. 4, where the rotational strength of the 2.02 eV transition has an opposite sign with the second parallel-polarized transition, and this character is also shown in the experimental spectrum [26,27]. However, since the depolarization effect is not included in the paper, it is difficult to assert which assignment is correct.

In Fig. 4, the cross-polarized transitions in absorption and CD spectra with different next-nearest-neighbor hopping couplings are simulated and shown. The parallel-polarized transitions are not shown here since the variation of the next-nearest-neighbor hopping coupling does not affect the characters. The result is expected. As mentioned in Sec. II D, the next-nearest-neighbor hopping coupling introduces electron-hole asymmetry into the band structure by equivalently adding a sinusoidal function of $\mathbf{k}$ to the conduction and valence band structures. Given the excitation matrix in Eq. (67), the parallel-polarized exciton, which is given by the selection rule $\mathbf{k} = 0$, is thus not modified with the asymmetry, and the cross-polarized exciton, which is given by the selection rule $\mathbf{k} = \pm\boldsymbol{\phi}$, is modified. It is interesting to note that, with each other without the next-nearest-neighbor hopping coupling, opposite-sign rotatory transitions around 2.02 eV in the CD are canceled. But within a range of the next-nearest-neighbor hopping coupling, the transitions are splitting and the rotational dispersion can be observed.

Additionally, we also simulate the CD of (11,−5)−SWNT, which is conventionally assigned as an enantiomer of (6,5)−SWNT, and the result is shown in Fig. 3(c). As can be seen in the figure, the two spectra are similar in characteristic peaks with opposite signs but are not identical. It is because the two structures are actually not the exact mirror image of each other in the present coordinate construction. A small geometry distortion of (11,−5)−SWNT away from the mirror image of (6,5)−SWNT exists due to the definition of the basis vector $\mathbf{b}_0$ in the beginning of geometry construction and the chirality-induced inequivalent length among the three vectors pointing to three nearest-neighbor sites on a rolled-up SWNT. As introduced in Sec. II C, the basis vectors of both SWNTs are assumed to be $\mathbf{b}_0 = -(\mathbf{a}_1 + \mathbf{a}_2)/3$. However, since the chiral number "m" of (11,−5)−SWNT is a negative number, the basis vector of (11,−5)−SWNT has to be changed to $\mathbf{b}_0 = (-\mathbf{a}_1 + 2\mathbf{a}_2)/3$ such that the geometry could be ensured to be the mirror image of the (6,5)−SWNT with the original definition of $\mathbf{b}_0$. Because of the chirality-induced geometry distortion, the mirror symmetry of two structures is broken. In Fig. 3(c), the difference of the two spectra is mainly on the cross-polarized transition around 2.8 eV, and it might imply that the corresponding exciton is susceptive to small geometry distortion.

B. Exciton spectra of different SWNTs

In the section, the exciton spectra of four additional SWNTs with different chiral indices are studied. In Fig. 5, the calculated absorption and CD spectra of SWNTs with different chiral

indices including three semiconducting (6,4), (7,5), (8,4) and one quasimetallic (9,6) SWNTs are shown. As in the case of (6,5)−SWNT, the parallel-polarized transitions in the absorption spectra have good comparison with the experiments, and the unexpected strong absorption of cross-polarized excitons are observed [26,27]. However, the CD spectra are not all described so well. Particularly, the signs of the third and forth excitonic transitions of (6,4)−SWNT in the CD spectrum are incorrectly predicted. By a noninteracting limit calculation, we have found that the incorrectness of the sign prediction already exists. While density-functional theory calculations had been reported to predict the signs correctly [25,55], the discrepancy can only be attributed to the roughness of the present model and method on the band structure calculation. Effects which are not considered in the present work, such as third-nearest-neighbor hopping coupling, σ-π mixing, and electron correlation, might result in the reversed sign prediction. For other spectra, the simulations are roughly corresponding to the reports [26,27]. The signs of the CD spectra of type-I ($\mathrm{mod}(|n-m|,3)=1$) and type-II ($\mathrm{mod}(|n-m|,3)=2$) semiconducting SWNTs are opposite to each other [56]. While the characters of the spectra with the same polarization and the same type are similar, the difference in relative positions of the parallel-polarized and cross-polarized transitions decide the variation of each spectrum.

In a short summary for the last two sections, even though there are some minor inconsistencies in the simulation, the present exciton calculations assisted still provide a quantitatively good match with experimental spectra. It is important to note that either the model or the theoretical method in the present paper is extremely simplified in comparing with the real situation. Therefore, it is impossible to use a single set of parameters to predict every physical quantity accurately. We have pointed out the possible reasons to cause the discrepancies, and we expect it could be helpful if there will be any followup work to improve the present formalism. Built on the finite success, different properties of SWNTs related to optical activity can be studied and predicted. In the following two sections, the magnetic optical activity of (6,5)−SWNT is studied as an example.

C. Aharonov-Bohm effect and dark exciton

In this section, the exciton spectra of (6,5)−SWNT in a uniformly axial magnetic field are studied, and the Aharonov-Bohm effect is discussed. In Fig. 6, the absorption and CD spectra of (6,5)−SWNT are simulated under different magnitude of axial magnetic fields. For the parallel-polarized transitions, as can be seen in Fig. 6(a), the Aharonov-Bohm effect is observed in the absorption spectra as the emerging dark-exciton transitions and splittings of the resonance peaks. As the usual explanation, the emerging dark exciton is attributed to the time-reversal symmetry breaking and the splitting is attributed to the magnetic-flux-induced band-energy shifts [38–40]. However, in the reported spectra, the peak position of the second dark-exciton transition is supposed to be higher in resonance energy than the second bright-exciton transition [44,45]. It is contrary to the present calculation that the peak position is lower. It indicates that the present calculation is not able to find correct order of the second dark/bright exciton

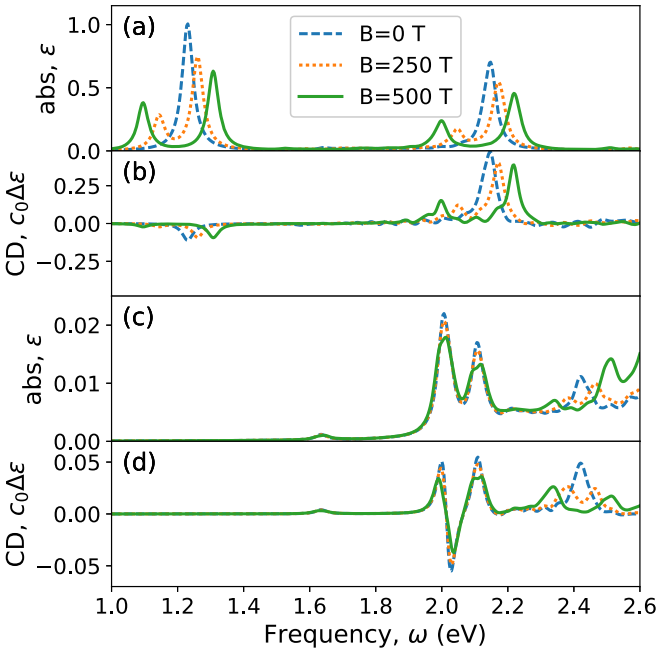

FIG. 6. Calculated absorption and CD spectra of (6,5)−SWNT without and with an axial magnetic field. (a) parallel-polarized transitions in absorption spectrum; (b) cross-polarized transitions in absorption spectrum; (c) parallel-polarized transitions in CD spectrum; (d) cross-polarized transitions in CD spectrum given by Eq. (22). The linewidth is 0.02 eV.

pair. While it is known that the order of the dark/bright exciton is related to the relative strengths of short-range Coulomb interactions [39], the discrepancy might be attributed to some electron correlation effects that we do not include, such as dielectric screening effect and σ-electron polarization.

On the other hand, in Fig. 6(b), the Aharonov-Bohm effect in the CD spectrum appears with similar characters with one in the absorption spectra. It implies that the dark excitons share the same optical activity with the associate bright excitons. For the cross-polarized transitions, the CD spectrum is given by Eq. (22) and the Faraday-effect contribution is not considered in order to focus on the discussion of dark-bright exciton splitting. As shown in Figs. 6(c) and 6(d), the dark-bright exciton splitting of the lowest few transitions are barely observed, while the splitting of the higher-energy transitions near 2.4 eV are still obvious. The scarcely-splitting cross-polarized transitions might be assigned as the transitions from the valence-band valley to the conduction-band valley with the same direction of increasing or decreasing the band energies under an axial magnetic field. The equivalent in the direction of band-energy shifts results in a weaker excitation-energy shift, and thus the dark-bright exciton splitting becomes barely observed.

D. Faraday effect and circular polarization

Although we have given the CD spectrum of cross-polarized exciton in an axial magnetic field in Fig. 6(d), the magnetic-field effect is actually difficult to be observed because the rotational strength under a strong magnetic field is mainly given by the nondiagonal term of polarizability tensor in

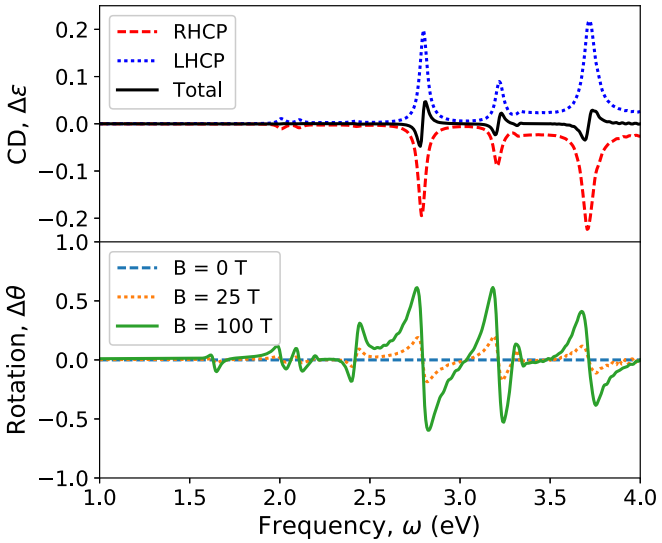

FIG. 7. Up: calculated cross-polarized transitions in CD spectra of (6,5)−SWNT with an axial magnetic field of $\mathcal{B} = 25$ Tesla by Eq. (23) or Eq. (69). The dash line is the contribution of right-handed circular polarization (RHCP) and dot line is the contribution of left-handed circular polarization (LHCP), and the solid line is their combination. Down: the degree of rotation of cross-polarized exciton with different magnitudes of axial magnetic fields. The linewidth is 0.02 eV.

Eq. (23). If the dipole-moment operator is rewritten by $\hat{\boldsymbol{\mu}} = \hat{\mu}^{+}\mathbf{e}_{+} + \hat{\mu}^{-}\mathbf{e}_{-} + \hat{\mu}^{\parallel}\mathbf{e}_{3}$ and then the polarizability tensor can be transformed into the frame spanned by the Jones vectors, Eq. (23) can be rewritten as

$$\begin{aligned}\Delta\epsilon_{\mathrm{CP},2}(\omega) &= 2\nu_0\omega\mathrm{Im}[\alpha^{+-}(-\omega;\omega) - \alpha^{-+}(-\omega;\omega)] \\ &= \epsilon_{\mathrm{LHCP}}(\omega) - \epsilon_{\mathrm{RHCP}}(\omega),\end{aligned} \tag{69}$$

which is the difference of the absorption spectra of left-handed circularly-polarized exciton (ϵ_{LHCP}) and right-handed circularly-polarized exciton (ϵ_{RHCP}). A degree of rotation is defined as

$$\Delta\theta(\omega) = \frac{\epsilon_{\mathrm{RHCP}}(\omega) - \epsilon_{\mathrm{LHCP}}(\omega)}{\epsilon_{\mathrm{RHCP}}(\omega) + \epsilon_{\mathrm{RHCL}}(\omega)} = -\frac{\Delta\epsilon_{\mathrm{CP},2}(\omega)}{\epsilon_{\mathrm{CP}}(\omega)}. \tag{70}$$

In the up panel of Fig. 7, the contribution of the two handedness-selected cross-polarized excitons to the CD spectrum of (6,5)−SWNT under an axial magnetic field of 25 Tesla is shown. In the down panel of Fig. 7, the degrees of rotation are shown with different magnitudes of the magnetic field. As shown in the figure, without the magnetic field, the absorption spectra of right-handed and left-handed excitons are identical, resulting in the complete cancellation of the rotational strengths in CD spectrum and the zero degree of rotation for the whole frequency range. On the other hand, with a finite magnetic field, the cancellation becomes incomplete and the rotational dispersion emerges. The incomplete cancellation can be explained by the opposite momentum transfer for the selection rules of handed excitons in Eq. (56) and the asymmetrically distorted helical band structure under the magnetic field. It is known as interband Faraday effect [48,50–52].

Different to the magnetic-field effect mentioned in Sec. III C, which is about the dark-bright-exciton splitting under an axial magnetic field, the interband Faraday effect is a bright-bright-exciton splitting of two handedness. It is needed to note that the magnitude of rotational strength in the up panel of Fig. 7 is measured by $\Delta\varepsilon$, which is different to others with a c_0 factor and thus is about two orders of magnitude larger in strength with the same digital number. It is shown that, even with much weaker magnetic field, the rotational strength given by Eq. (23) is much larger than the one given by Eq. (22). Only for extremely weak magnetic field the contribution from Eq. (22) will win, where with the magnetic field the dark-bright-exciton splitting would be smaller than the linewidth of the absorption peak and be unobservable. It ensures interband Faraday effect to be the major contribution to optical activity in SWNTs for a wide range of the magnetic field.

IV. CONCLUSION

In conclusion, we have used the helical-rotational symmetry to solve the helical band structures and derive the matrix elements of SWNTs under the tight-binding approximation. While the Coulomb interaction is considered, the band structure is solved by Hartree-Fock approximation and the exciton state is given by singly-excited configuration interaction method. By using those techniques, the simulated exciton spectra including optical absorption and CD are found good correspondence with experimental reports. The effects of electron-hole asymmetry and axial magnetic-field interaction on the spectra can be analyzed based on the helical band structures and the selection rules. However, the present model and method still have some insufficiencies to accurately describe the spectra due to lack of considering such as electron correlation on band structures, σ-π mixing, and depolarization effect.

ACKNOWLEDGMENTS

We wish to acknowledge the financial support from the Ministry of Science and Technology, Taiwan, ROC and the Center of Theoretical Sciences of National Taiwan University. We thank the useful discussions with Dr. Yuan-Jia Fan and Prof. Yuan-Chung Cheng.

[1] R. Saito, G. Dresselhaus, and M. S. Dresselhaus, *Physical Properties of Carbon Nanotubes* (Imperial College Press, London, 1998).

[2] P. Avouris, M. Freitag, and V. Perebeinos, Nat. Photon. **2**, 341 (2008).

[3] L. Ren, C. L. Pint, L. G. Booshehri, W. D. Rice, X. Wang, D. J. Hilton, K. Takeya, I. Kawayama, M. Tonouchi, R. H. Hauge, and J. Kono, Nano Lett. **9**, 2610 (2009).

[4] J.-H. Han, G. L. C. Paulus, R. Maruyama, D. A. Heller, W.-J. Kim, P. W. Barone, C. Y. Lee, J. H. Choi, M.-H. Ham,

C. Song, C. Fantini, and M. S. Strano, Nat. Mater. **9**, 833 (2010).
[5] S. Nanot, E. H. Hároz, J.-H. Kim, R. H. Hauge, and J. Kono, Adv. Mater. **24**, 4977 (2012).
[6] S. M. Bachilo, M. S. Strano, C. Kittrell, R. H. Hauge, R. E. Smalley, and R. B. Weisman, Science **298**, 2361 (2002).
[7] R. B. Weisman and S. M. Bachilo, Nano Lett. **3**, 1235 (2003).
[8] C. Fantini, A. Jorio, M. Souza, M. S. Strano, M. S. Dresselhaus, and M. A. Pimenta, Phys. Rev. Lett. **93**, 147406 (2004).
[9] G. Dukovic, F. Wang, D. Song, M. Y. Sfeir, T. F. Heinz, and L. E. Brus, Nano Lett. **5**, 2314 (2005).
[10] S. R. Sanchez, S. M. Bachilo, Y. Kadria-Vili, C.-W. Lin, and R. B. Weisman, Nano Lett. **16**, 6903 (2016).
[11] E. Chang, G. Bussi, A. Ruini, and E. Molinari, Phys. Rev. Lett. **92**, 196401 (2004).
[12] J. Jiang, R. Saito, Ge. G. Samsonidze, A. Jorio, S. G. Chou, G. Dresselhaus, and M. S. Dresselhaus, Phys. Rev. B **75**, 035407 (2007).
[13] M. S. Dresselhaus, G. Dresselhaus, R. Saito, and A. Jorio, Annu. Rev. Phys. Chem. **58**, 719 (2007).
[14] J. Deslippe, M. Dipoppa, D. Prendergast, M. V. Moutinho, R. B. Capaz, and S. G. Louie, Nano Lett. **9**, 1330 (2009).
[15] H. Ajiki, J. Phys.: Condens. Matter **24**, 483001 (2012).
[16] S. Choi, J. Deslippe, R. B. Capaz, and S. G. Louie, Nano Lett. **13**, 54 (2012).
[17] H. Liu, S. Schumacher, and T. Meier, Phys. Rev. B **89**, 155407 (2014).
[18] L. Rosenfeld, Z. Phys. **52**, 161 (1928).
[19] E. U. Condon, Rev. Mod. Phys. **9**, 432 (1937).
[20] A. D. Buckingham and P. J. Stiles, Acc. Chem. Res. **7**, 258 (1974).
[21] I. Warnke and F. Furche, WIREs Computational Molecular Science **2**, 150 (2012).
[22] X. Peng, N. Komatsu, S. Bhattacharya, T. Shimawaki, S. Aonuma, T. Kimura, and A. Osuka, Nat. Nanotech. **2**, 361 (2007).
[23] A. A. Green, M. C. Duch, and M. C. Hersam, Nano Research **2**, 69 (2009).
[24] S. Ghosh, S. M. Bachilo, and R. B. Weisman, Nat. Nanotech. **5**, 443 (2010).
[25] C. Noguez and F. Hidalgo, Chirality **26**, 553 (2014).
[26] G. Ao, J. K. Streit, J. A. Fagan, and M. Zheng, JACS **138**, 16677 (2016).
[27] X. Wei, T. Tanaka, Y. Yomogida, N. Sato, R. Saito, and H. Kataura, Nat. Commun. **7**, 12899 (2016).
[28] Y. Miyauchi, M. Oba, and S. Maruyama, Phys. Rev. B **74**, 205440 (2006).
[29] S. Kilina, S. Tretiak, S. K. Doorn, Z. Luo, F. Papadimitrakopoulos, A. Piryatinski, A. Saxena, and A. R. Bishop, Proc. Natl. Acad. Sci. U.S.A. **105**, 6797 (2008).
[30] K.-C. Chuang, A. Nish, J.-Y. Hwang, G. W. Evans, and R. J. Nicholas, Phys. Rev. B **78**, 085411 (2008).
[31] S. Uryu and T. Ando, Phys. Rev. B **74**, 155411 (2006).
[32] Z. Wang, H. Zhao, and S. Mazumdar, Phys. Rev. B **76**, 115431 (2007).
[33] S. Uryu and T. Ando, Phys. Rev. B **83**, 085404 (2011).
[34] S. Uryu and T. Ando, J. Phys. Conf. Ser. **302**, 012004 (2011).
[35] S. Uryu and T. Ando, Phys. Rev. B **86**, 125412 (2012).
[36] H. Ajiki and T. Ando, Physica B: Condensed Matter **201**, 349 (1994).
[37] J. P. Lu, Phys. Rev. Lett. **74**, 1123 (1995).
[38] T. Ando, J. Phys. Soc. Jpn. **73**, 3351 (2004).
[39] T. Ando, J. Phys. Soc. Jpn. **75**, 024707 (2006).
[40] S. Uryu and T. Ando, Phys. Rev. B **76**, 115420 (2007).
[41] S. Zaric, G. N. Ostojic, J. Kono, J. Shaver, V. C. Moore, M. S. Strano, R. H. Hauge, R. E. Smalley, and X. Wei, Science **304**, 1129 (2004).
[42] S. Zaric, G. N. Ostojic, J. Shaver, J. Kono, O. Portugall, P. H. Frings, G. L. J. A. Rikken, M. Furis, S. A. Crooker, X. Wei, V. C. Moore, R. H. Hauge, and R. E. Smalley, Phys. Rev. Lett. **96**, 016406 (2006).
[43] S. Takeyama, H. Suzuki, H. Yokoi, Y. Murakami, and S. Maruyama, Phys. Rev. B **83**, 235405 (2011).
[44] W. Zhou, D. Nakamura, H. Liu, H. Kataura, and S. Takeyama, Sci. Rep. **4**, 6999 (2014).
[45] D. Nakamura, T. Sasaki, W. Zhou, H. Liu, H. Kataura, and S. Takeyama, Phys. Rev. B **91**, 235427 (2015).
[46] E. L. Ivchenko and B. Spivak, Phys. Rev. B **66**, 155404 (2002).
[47] G. G. Samsonidze, A. Grüneis, R. Saito, A. Jorio, A. G. Souza Filho, G. Dresselhaus, and M. S. Dresselhaus, Phys. Rev. B **69**, 205402 (2004).
[48] A. Zarifi and T. G. Pedersen, Phys. Rev. B **77**, 085409 (2008).
[49] J. Have and T. G. Pedersen, Phys. Rev. B **97**, 115405 (2018).
[50] B. Lax and Y. Nishina, Phys. Rev. Lett. **6**, 464 (1961).
[51] I. M. Boswarva, R. E. Howard, and A. B. Lidiard, Proc. R. Soc. London A **269**, 125 (1962).
[52] T. G. Pedersen, Phys. Rev. B **68**, 245104 (2003).
[53] S. Tasaki, K. Maekawa, and T. Yamabe, Phys. Rev. B **57**, 9301 (1998).
[54] A. Sánchez-Castillo, C. E. Román-Velázquez, and C. Noguez, Phys. Rev. B **73**, 045401 (2006).
[55] A. Sánchez-Castillo and C. Noguez, J. Phys. Chem. C **114**, 9640 (2010).
[56] N. Sato, Y. Tatsumi, and R. Saito, Phys. Rev. B **95**, 155436 (2017).
[57] L. Pauling, R. B. Corey, and H. R. Branson, Proc. Natl. Acad. Sci. U.S.A. **37**, 205 (1951).
[58] P. W. Higgs, Proc. R. Soc. A **220**, 472 (1953).
[59] W. Moffitt, J. Chem. Phys. **25**, 467 (1956).
[60] F. M. Loxsom, J. Chem. Phys. **51**, 4899 (1969).
[61] C. W. Deutsche, J. Chem. Phys. **52**, 3703 (1970).
[62] A. I. Levin and I. Tinoco Jr., J. Chem. Phys. **66**, 3491 (1977).
[63] C. T. White, D. H. Robertson, and J. W. Mintmire, Phys. Rev. B **47**, 5485 (1993).
[64] E. B. Barros, A. Jorio, G. G. Samsonidze, R. B. Capaz, A. G. Souza Filho, J. Mendes Filho, G. Dresselhaus, and M. S. Dresselhaus, Phys. Rep. **431**, 261 (2006).
[65] V. A. Margulis and E. E. Muryumin, Physica B: Condensed Matter **405**, 1796 (2010).
[66] W. Izumida, R. Okuyama, A. Yamakage, and R. Saito, Phys. Rev. B **93**, 195442 (2016).
[67] R. Pariser and R. G. Parr, J. Chem. Phys. **21**, 466 (1953).
[68] J. A. Pople, Trans. Faraday Soc. **49**, 1375 (1953).
[69] L. Salem, *Molecular Orbital Theory of Conjugated Systems* (W. A. Benjamin, Inc., New York, 1966).
[70] J. Callaway, *Quantum Theory of the Solid State: Part B* (Academic Press, Inc., New York, 1974).
[71] M. Graf and P. Vogl, Phys. Rev. B **51**, 4940 (1995).
[72] J. Linderberg and L. Seamans, Int. J. Quantum Chem. **8**, 925 (1974).

[73] P. R. Nagy, P. R. Surján, and Á. Szabados, J. Chem. Phys. **140**, 044112 (2014).

[74] See Supplemental Material at http://link.aps.org/supplemental/10.1103/PhysRevB.97.205413 for the detailed derivation of the multipolar expansion, the derivation of the two contributions in the rotational strength, and the detail of using the coupled-perturbed Hartree-Fock equation to solve the matrix elements in exciton theory.

[75] P. Otto, F. L. Gu, and J. Ladik, J. Chem. Phys. **110**, 2717 (1999).

[76] S. Hirata, M. Head-Gordon, and R. J. Bartlett, J. Chem. Phys. **111**, 10774 (1999).